Performance Characterization of Joint Communication and Sensing With Beyond 5G NR-V2X Sidelink

Nicolò Decarli, *Member, IEEE*, Stefania Bartoletti, *Member, IEEE*, Alessandro Bazzi, *Senior Member, IEEE*, Richard A. Stirling-Gallacher, *Member, IEEE*, and Barbara M. Masini, *Senior Member, IEEE*

***Abstract*—Joint communication and sensing allows to share frequency spectrum, hardware, and signal processing blocks between communication and sensing, providing new radar functionalities through the exploitation of communication signals. This is becoming an important trend also in vehicular communications, where future standardized technologies for connected vehicles can be used to detect targets nearby without overloading the already scarce spectrum with dedicated radar signals. Objective of this paper is to characterize the performance of 5G new radio (NR) vehicle-to-everything (V2X) sidelink, in terms of lower bounds for sensing purposes; specifically, we evaluate the impact of physical and radio access communication parameters on the sensing performance in terms of detection capability and parameter estimation quality. As a result, it is shown how the effect of the presence of multiple vehicles in the scenario, and the inherent resource allocation policies, have a non-negligible impact on the communication and sensing performance. In particular, it is shown that when considering the interference of multiple vehicles, the influence on sensing performance of the chosen radio parameters, such as bandwidth, modulation and coding scheme, and packet size is different compared to the inference free case.**

***Index Terms*—Joint communication and sensing (JCS), NR-V2X sidelink, vehicular communications, integrated sensing and communication (ISAC), joint radar and communication (JRC).**

I. Introduction

FUTURE vehicles will rely on advanced on-board connectivity to exchange information with the other vehicles, with other road actors (such as bikers and pedestrians) and with the infrastructure or the network, through vehicle-to-everything (V2X) communications. This will allow each vehicle to build the perception of the surrounding environment and increase safety and efficiency. A more complete knowledge of the driving environment can be built when vehicles share the information acquired by the on-board sensors, such as radar, cameras and light detection and ranging (LiDAR) to enable the so-called *collective perception*. These new applications will imply a strong convergence of automation and connectivity on-board and an increasing amount of generated data, resulting in a dramatic demand of data rate. Following Cisco forecast [1], automated vehicles will generate up to 80 GB of data per driven-hour from on-board sensors, accumulating 1.2 TB of data in a 16-hour day. Even if most of these data will be processed locally on-board of the vehicle, a non-negligible subset will be transmitted through V2X communications. If we assume as an example that connected vehicles transfer 8 GB per day, the data volume generated from vehicles will rapidly outstrip that of smartphones with an important stress on currently available V2X communication technologies, such as ITS-G5, which appear then insufficient [2]. Hence, to be fully effective, V2X communication will need to leverage the full capacity of 5G and beyond systems [3].

In this context of high data-rate communication and, at the same time, of spectrum scarcity, communication and sensing communities started working on spectrum sharing to efficiently use the scarce available resources. Specifically, joint communication and sensing (JCS) allows to share frequency spectrum, hardware architectures, and signal processing blocks between communication and sensing [4], [5], [6], [7], providing radar functionalities exploiting the communication signal already available for V2X communication.

When the vehicle performing sensing is the same which is transmitting a data packet (thus analyzing the response of the environment while transmitting), we are in presence of a so-called *monostatic radar*. In this configuration, where the transmitter and the receiver are co-located, it must be observed that the integration of sensing functionalities into communication devices requires proper modifications of the architectures adopted, such as the use of full-duplex radios to allow simultaneous transmission and reception at the expense of employing complex mechanisms to avoid mutual interference [8].[1]

Manuscript received 4 March 2023; revised 18 December 2023; accepted 16 January 2024. Date of publication 16 February 2024; date of current version 16 July 2024. This work was supported by WiLab-Huawei Joint Innovation Center. The review of this article was coordinated by Prof. Hongzi Zhu. *(Corresponding author: Nicolò Decarli.)*

Nicolò Decarli and Barbara M. Masini are with the National Research Council - Institute of Electronics, Computer and Telecommunication Engineering (CNR-IEIIT) and WiLab-CNIT, 40136 Bologna, Italy (e-mail: nicolo.decarli@cnr.it; barbara.masini@cnr.it).

Stefania Bartoletti is with the University of Rome "Tor Vergata" and WiLab-CNIT, 00185 Rome, Italy (e-mail: stefania.bartoletti@uniroma2.it).

Alessandro Bazzi is with the University of Bologna and WiLab-CNIT, 40136 Bologna, Italy (e-mail: alessandro.bazzi@unibo.it).

Richard A. Stirling-Gallacher is with the Munich Research Center, Huawei Technologies Duesseldorf GmbH, 40547 Düsseldorf, Germany (e-mail: richard.sg@huawei.com).

Digital Object Identifier 10.1109/TVT.2024.3365770

[1] Differently, if the receiver performing radar sensing is located on a different vehicle, a *bistatic* radar configuration is considered [9], and full-duplex radios are not required.

However, dealing with vehicles, hence with complex objects, the assumption of on-board embedded full-duplex radios with good self-interference cancellation is not far from reality. On the other hand, it is important to highlight that JCS enables radar capabilities for free on a standardized communication system. This is a very important aspect since, in spite new vehicles are being equipped with advanced monostatic radar sensors (e.g., radar sensors at 77 GHz), they do not follow unified standardization rules, providing different proprietary solutions. Since these radars have no resource allocation schemes for accessing the spectrum, but just fulfill spectral mask emission rules, this leads to uncontrolled interference, which can severely affect their sensing capability [10]. Such an issue is causing confusion and unnecessary challenges to be faced by consumers, car makers and administration entities. Despite some works addressed the coexistence among radars (see, e.g., the discussion in [11] and the references therein), we are still far from the convergence to an international standard. Differently, the use of JCS, thus exploiting the same signals used for communication, where specific resource allocation policies are considered to control the interference, could be a big advantage for future sensing compared to today's monostatic radars.

Examining the recent literature, it can be observed that there has been an increased interest on JCS for vehicular scenarios especially when 5G and beyond communication systems are considered. However, most of these works deal with solutions not specifically designed or dedicated to vehicular scenarios and vehicular wireless access technologies, and they rarely address the ITS band in the sub-6 GHz region. Several solutions, for example, have been proposed in the wide frequency range of mmWaves between 20 GHz and 80 GHz [12], [13], where the sharp beams obtained with multiple antennas [14], [15], [16] can be exploited for fine angular sensing; other works focus on infrastructure-based cellular network, evaluating the adoption of new wireless access techniques and consider the impact of resource allocation algorithms [17], [18]. A limited number of works, instead, investigate the sensing performance of technologies specifically dedicated to vehicular communications, mainly limited to IEEE 802.11p [19], [20], [21]. In contrast, papers specifically focused on vehicular wireless access technologies, such as [22], [23], [24], [25] do not consider JCS potentialities and challenges. To the best of the authors' knowledge, the recent literature does not properly investigate the impact of communication parameters, resource allocation modes, and interference on the sensing performance when the communication signal of a vehicular wireless access technology is considered, and this is especially true when referring to the latest 3GPP sidelink specifications in new radio (NR)-V2X sidelink.

In this paper, we evaluate the impact of physical and radio access communication parameters on JCS performance in NR-V2X sidelink. Specifically, we consider here the probability of detecting a passive target and the bounds on the parameters estimation accuracy both in the absence and in presence of multi-user interference. To this end, we propose an evaluation framework composed of a proper analytical model and a simulation approach. The analytical model is adopted for deriving closed-form expressions for the performance bounds of JCS in relationship with NR-V2X sidelink signal parameters; then, system-level simulations are exploited to characterize the impact of the scenario and parameters not accounted by the analytical model itself, with particular emphasis on the effect of multi-vehicle interference.

The main contributions of this work can be summarized as follows:

- We focus on JCS for vehicular wireless access technologies and, specifically, on NR-V2X sidelink. The main characteristics of the NR-V2X sidelink are revised and considered when evaluating the communication and sensing performance;
- We account for the presence of interference due to multi-user vehicular scenarios, highlighting the impact of resource allocation policies in realistic traffic conditions.

Moreover, to better position our work, we provide an extensive literature review concerning JCS in vehicular contexts. As an important outcome, we show that when considering the interference of multiple vehicles, the impact of the chosen radio parameters, such as bandwidth, modulation and coding scheme, and packet size, can be different for communication and sensing, and can change completely depending on the interference in the environment.

The paper is organized as follows: In Section II, the recent literature is reviewed; in Section III, the NR-V2X sidelink communication scheme is introduced and the resource allocation policies are described, by also comparing NR-V2X with other vehicular communication technologies. Then, in Section IV, the signal model is presented, and the sensing performance is analytically evaluated in terms of probability of target detection and Cramér-Rao Lower Bound (CRLB) on the variance of the estimation error for the target range and speed; then, the multi-user scenario is introduced, by presenting a method for the performance evaluation in the presence of interference based on system-level simulations. Extensive results are proposed in Section V, where simulations performed in a realistic highway scenario are discussed. Finally, our conclusions are drawn in Section VI.

II. Related Works

Recent literature related to JCS in vehicular scenarios has the following main limitations: *(i)* most works deal with generic radar sensing at different frequencies without focusing on sidelink wireless access technologies; *(ii)* the impact of interference is rarely considered; and *(iii)* the impact of autonomous resource allocation has not been explored.

In Table I we summarize several recent works on JCS in vehicular scenarios and highlight their main characteristics. As it can be observed, most of the works deal with automotive radar sensing and communication using mmWaves in the range of 60–80 GHz. Even if these works are not based on vehicular wireless communication technologies, the same waveform is adopted for both communication and sensing [26], [27], [28], [29], [30], [31]. Specifically, in [26], Kumari et al. formulate an integrated framework to study vehicle-to-vehicle (V2V) communication and long-range radar based on IEEE 802.11ad standard at

TABLE I
SUMMARY OF THE MAIN CHARACTERISTICS OF RECENT PAPERS ON JOINT COMMUNICATION AND SENSING IN VEHICULAR SCENARIOS

Reference	Carrier	V2X technology	Main focus
Kumari, 2018 [26]	60 GHz	mmWaves/IEEE 802.11ad	Proposal of a joint vehicular communication and radar system reusing the same waveform for long range automotive radar to exploit the same spectrum and to leverage shared hardware.
Kumari, 2021 [27]	57-70 GHz	mmWaves/IEEE 802.11ad	Proposal of an adaptive combined waveform-beamforming design for a mmWave automotive joint communication and radar systems to trade-off between communication and radar performance.
Ozkaptan, 2018 [28]	76-81 GHz	mmWaves	Design of a JCS system for vehicles using the same waveform.
Ozkaptan, 2019 [29]	76-81 GHz	mmWaves	Proof of concept that uses pilot symbols for radar sensing while simultaneously transmitting communication symbols in data subcarriers.
Wang, 2020 [30]	76-81 GHz	mmWaves	Proposal of a multi-range joint automotive radar and communication system exploiting dynamic allocation of pilot subcarriers to switch between radar specifications.
Lubke, 2020 [31]	77 GHz	General	Proposal of a system that combines radar sensing and communication using direct sequence spread spectrum signals.
Liyanaarachchi, 2021 [13]	27.7 GHz	mmWaves in 5G-NR	Simulation and over the air measurements with default and optimized 5G NR waveforms.
Wild, 2021 [12]	N/A	mmWaves in 5G-NR	Design aspects for the adoption of integrated sensing and communication (ISAC) in cellular systems. Discussion on the choice of the waveform and on techniques for efficient integration.
Petrov, 2019 [32]	N/A	mmWaves in 5G-NR	Proposal of an approach to harmonizing automotive radar sensing and V2X operating in mmWave frequencies.
Liu, 2020 [33]	N/A	mmWaves	Proposal of a radar-assisted predictive beamforming design for V2I communication by exploiting the dual-functional radar-communication (DFRC).
Liu, 2020 [34]	General model	General OFDM system	Proposal of an auto-paired super-resolution range and velocity estimation method by using the OFDM integrated radar and communications waveform.
Yuan, 2021, [4]	N/A	N/A	Proposal of an ISAC technique for assisting OTFS transmission in both uplink and downlink V2I communication to enable the estimation of motion parameters.
Khan, 2021 [17]	N/A	Beyond 5G networks	Analysis for NOMA-enabled backscatter-based V2X networks considering the downlink of a legacy cellular systems with intermediate RSUs.
Dokhanchi, 2021 [17]	N/A	General	Single data stream in a multi-vehicle scenario with the aim at detecting multiple targets.
Zhang, 2021 [39]	28 GHz	mmWaves	Dynamic resource allocation mechanism for TDD operations to support JCS.
Barneto, 2020 [40]	28 GHz	mmWaves	Power split between communication beams and a sensing beam.
Ozkaptan, 2021 [36]	76-81 GHz	mmWaves	Design of a precoding vector enabling beamforming and radar imaging in a multi-user scenario, using MIMO-OFDM JCS.
Ni, 2022 [37]	35 GHz	mmWaves	Proposal of a frequency modulated continuous wave (FMCW) radar based on frequency-hopping to trade between communication and sensing performance.
Wang, 2021 [38]	30 GHz	mmWaves	Multi-beam technique to provide short-range and long-range sensing of multiple targets in V2V scenarios, accounting for interference of sensing signals.
Kihei, 2015 [20]	5.9 GHz	IEEE 802.11p	Simulation of collision avoidance radar considering 802.11p waveform as a multi-frequency continuous wave radar.
U. Mazher, 2018 [21]	5.9 GHz	IEEE 802.11p	Simulation of vehicular radar considering two antennas at receiver for direction-of-arrival estimation.
Reichardt, 2012 [19]	5.9 GHz	IEEE 802.11p	Simulations and field trials of the use of IEEE 802.11p signals for joint radar and communication, proposing the use of adjacent channels to improve the radar performance.
Bartoletti, 2022, [41], [42]	5.9 GHz	5G-V2X	Preliminary works on the impact of resource allocation on the sensing performance.

60 GHz, achieving promising performance in terms of detection probability. To further improve the performance, the adoption of multiple input multiple output (MIMO) systems is foreseen, and an adaptive and fast combined waveform-beamforming that uses a phased-array architecture is proposed in [27]. Also Ozkaptan et al. focus on automotive radar in [28], [29] and specifically in the range 76–81 GHz, proposing radar processing methods that use pilots in the orthogonal frequency-division multiplexing (OFDM) signal, such that while the radar receiver exploits pilots for sensing, the communication receiver can leverage pilots to estimate the time-varying channel. The same frequency range is considered by Wang et al. in [30] but, in this case, to switch between radar specifications for different ranges and minimize the age of information of the covered regions, the communication data rate based on traffic load is dynamically adjusted. Remaining in a similar frequency range, Lübke [31] modulates radar signals at 77 GHz to exchange safety information of the incoming surroundings between cars.

The same waveform for both communication and sensing is considered in some papers related to 5G NR; for example, Liyanaarachchi et al. in [13] study an optimized waveform at the mmWave band of 27.7 GHz. Interesting overviews are proposed by Wild et al. in [12] with focus on 5G NR and 6G for a worthwhile discussion on potential waveform for JCS in vehicle-to-infrastructure (V2I) communications where sensing is performed at the base station and by Petrov et al. in [32] to argue on unified channel access for mmWave vehicular communications and radar sensing. V2I is addressed also by F. Liu in [33] where a radar-assisted predictive beamforming design is presented by exploiting the dual-functional radar-communication technique aiming for realizing JCS functionalities at roadside units (RSUs).

To improve the resolution of range and velocity estimations in JCS, Y. Liu et al. in [34] propose a novel estimation method using a general OFDM system for vehicular scenarios, by first compensating the communication information in the received signal and then performing frequency smoothing to reduce the correlation between the echoes reflected by different targets. Cheng et al. in [35] introduce the concept of signaling JCS with either unified hardware or separate hardware platforms by highlighting the issues arising in several transportation case studies. Other recent works deal with the proposal of new waveforms for V2I JCS: Yuan et al. in [4] use orthogonal time frequency space (OTFS) modulation for supporting reliable transmissions in high-mobility vehicular scenarios and enable the RSU to estimate kinematic parameters of vehicles while transmitting information and, thus, build the network topology that can, then, be used in the uplink to infer the delays and dopplers associated with different channel paths, whereas Khan et al. in [17] focus on non-orthogonal multiple access (NOMA) to enable backscatter-based V2I networks. Some works consider also the presence of interference [36], [37], [38], but without resorting to a specific V2X communication technology.

Few works focus on sub-6 GHz vehicular technologies using the V2X sidelink communication signal also for sensing purposes, and they mainly assume the IEEE 802.11p [19], [20], [21]. In [20], Kihei et al. consider the IEEE 802.11p waveform as a multi-frequency continuous wave signal to estimate the velocity and range of non-connected vehicles. Sub-meter accuracy in location estimation is demonstrated by Mazher in [21] based on a two-path channel model with the first cluster corresponding to direct signal interference and the second cluster corresponding to the signal reflected from the target. Methods to improve IEEE 802.11p resolution and accuracy are proposed by Reichardt et al. in [19] both by simulations and field trials.

To the best of our knowledge, no work in the literature focuses on JCS for the 5G NR-V2X sidelink [25]. Although several recent papers provided deep insight on LTE-V2X and NR-V2X, such as [22], [23], [24], [25], they do not specifically consider JCS. Hence, differently from the rest of the literature, objective of this work is to focus on the 5G NR-V2X sidelink, and to investigate the impact of the physical and radio access channel parameters (such as the bandwidth, the packet dimension, the modulation scheme, etc.) and of the resource allocation policies on the sensing accuracy in realistic vehicular conditions.

III. NR-V2X Sidelink

The development of radio access technologies to enable reliable and low-latency V2X communications has become of paramount importance. Two families of wireless access technologies are under consideration for implementation on board to enable V2X communications. On one side, we encounter the solutions based on IEEE 802.11p and the more recent IEEE 802.11bd, stemming from the evolution of Wi-Fi standards tailored for vehicular environments. This includes dedicated short range communication (DSRC) in the US or ITS-G5 in Europe. On the other side, we have the 3GPP cellular-V2X (C-V2X) family, encompassing LTE-V2X, 5G NR-V2X [43], and the future 6G-V2X. Comparisons of these families, which rely on very different physical layer settings, frame structure, and access protocols, can be found in [43], [44], [45].

Among the cellular technologies, NR-V2X has been designed from the beginning for advanced services, opening the road to the expected growth of autonomous vehicles and the demand of new data hungry applications (such as, holographic control display systems, or immersive driving). It has indeed been the first V2X communication technology that tried to systematically integrate and support connected and autonomous vehicles (CAVs) scenarios, by defining clear use cases [46] and the related network requirements [47]. Several works have already comprehensively described NR-V2X specifications [2], [23]. Hence, in this section, we highlight the most salient features of 3GPP specifications for the sidelink, which are needed to set the ground for a proper understanding of the proposed model for JCS performance characterization.

A. Waveform and Radio Resources

As the other wireless access technologies for vehicular networks, NR-V2X is also based on OFDM at the physical (PHY) layer. Specifically, NR-V2X sidelink transmissions use cyclic prefix OFDM (CP-OFDM). In NR-V2X, higher modulation formats and LDPC codes can be adopted with respect to LTE-V2X, such as 64-quadrature amplitude modulation (QAM) and

TABLE II
NR-V2X NUMEROLOGY AND FREQUENCY RANGES

μ	Δf [kHz]	T_{sym} [ms]	slot duration [ms]	#slot/subframe	frequency	$W_{\text{ch}}^{\max}$ [MHz]
0	15	66.6	1	1	FR1	50
1	30	33.3	0.5	2	FR1	100
2	60	16.6	0.25	4	FR1, FR2	200
3	120	8.3	0.125	8	FR2	400

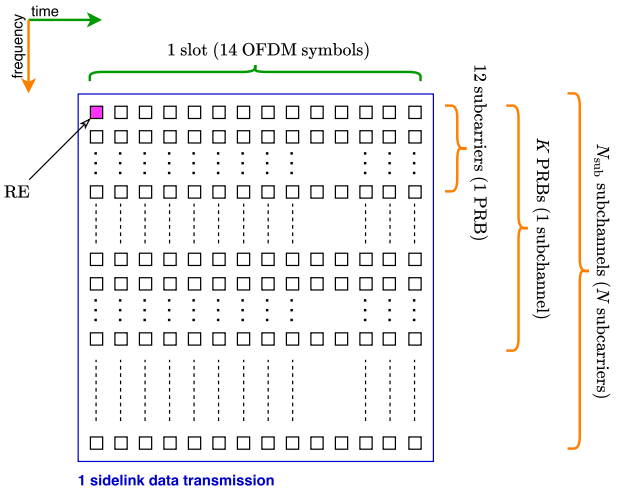

Fig. 1. Time-frequency structure of radio resources in NR-V2X.

256-QAM in addition to quadrature phase shift keying (QPSK) and 16-QAM, with binary reflected Gray mapping to enable increased spectral efficiency and throughput at the expense of sidelink coverage.

At the PHY layer, the NR-V2X radio resources (RRs) cover time and frequency domain. One subcarrier over one OFDM symbol defines the single resource element (RE). In the time domain, RRs are organized in frames and subframes of fixed duration equal to 10 ms and 1 ms, respectively. Each subframe is divided into one or more slots, each composed of 14 OFDM symbols when the standard cyclic prefix is adopted. The slot, also called transmission time interval (TTI), represents the granularity for resource allocation in the time domain. In the frequency domain, RRs are organized into physical resource blocks (PRBs) and subchannels. A PRB consists of 12 consecutive subcarriers with subcarrier spacing (SCS), Δf; as the SCS changes, the bandwidth of a PRB varies accordingly. A subchannel consists of K consecutive PRBs, where K can be selected among 10,12,15,20,25,50,75,100. The subchannel (i.e., K consecutive PRBs) represents the smallest resource allocation unit in the frequency domain.

One sidelink data transmission to be used for JCS is therefore composed of a slot in the time domain and N_{sub} contiguous subchannels in the frequency domain, depending on the size of the packet to transmit and the chosen modulation and coding scheme (MCS); the choice of the MCS in fact impacts the number of PRBs needed for accommodating the packet (lower MCS index, higher number of PRBs). Thus, one sidelink data transmission occupies $M = 14$ OFDM symbols and $N = 12\,K N_{\text{sub}}$ subcarriers, as for LTE-V2X (see Fig. 1).

B. NR Numerology

Differently from the fixed SCS used in LTE-V2X, NR-V2X introduces a scalable numerology, where the SCS values are flexible and follow the law $2^{\mu} \cdot 15$ kHz (with $\mu = 0, 1, 2, 3$), allowing subcarrier spacing Δf from 15 to 120 kHz. The corresponding symbol and slot duration, as well as the number of slots per subframe, are reported in Table II. Consequently, with the increasing of the SCS, Δf:

- The slot duration decreases, and the number of slots per subframe (equal to 2^{μ}) increases;
- The bandwidth of a PRB increases, thus the number of subchannels in a given radio channel decreases, possibly requiring the adoption of higher MCSs to accommodate the same data.

When using larger SCS, we have a shorter slot duration and hence, lower latency and higher resistance against doppler effect and carrier frequency offset at high vehicular speeds. In addition, by increasing the SCS, the number of subchannels in a given slot reduces and a lower number of UEs will transmit in a given slot, thus relaxing the half-duplex problem with respect to LTE-V2X [48], [49]. Furthermore, due to smaller slot duration at higher SCS, channel variations within the slot are typically smaller, implying that fewer demodulation reference signal (DMRS) symbols per slot for channel estimation are sufficient with respect to LTE-V2X. Also, flexible numbers of DMRS symbols per slot are allowed in NR-V2X.

As reported in Table II, the maximum bandwidth of the channel $W_{\text{ch}}^{\max}$ that can allocate sidelink transmissions changes with numerology. NR-V2X allows two frequency ranges: one between 410 MHz and 7.125 GHz, called frequency range 1 (FR1) or sub-6 GHz, where $\mu = 0, 1, 2$ can be used; the other between 24.25 GHz and 52.6 GHz, called frequency range 2 (FR2) or mmWave.

In this paper we consider classical FR1-based sidelink transmission and we account for $\mu = 0, 1, 2$ as possible values, leading to a maximum channel bandwidth of $W_{\text{ch}}^{\max} = 100$ MHz, according to Table II.[2] It is worth noticing that the number of PRBs needed to accommodate one packet does not change with the SCS; what changes is the transmission bandwidth $W \approx N\Delta f$ and the slot duration depending on the SCS Δf. The number of PRBs $N_{\text{PRB}}^{\star}$ needed to accommodate a packet of a given size is reported, for different MCSs, in Table III. Fixed the maximum channel bandwidth available W_{ch}, a physical limit on the maximum number of PRBs that can be accommodated for different SCSs arises. This number, denoted with $N_{\text{PRB}}^{\max}$ and

[2]Despite the maximum channel bandwidth allowed by the standard can reach 100 MHz in FR1, today's regulation often considers a maximum bandwidth of 10 MHz.

TABLE III
NUMBER OF PRBS NEEDED TO ACCOMMODATE A DATA PACKET OF A GIVEN SIZE

MCS	$N^{\star}_{\text{PRB}}$ (350 bytes)	$N^{\star}_{\text{PRB}}$ (1000 bytes)
0	107	292
1	82	224
2	68	183
3	53	141
4	44	116
5	36	95
6	31	81
7	27	69
8	24	61
9	22	54
10	22	54
11	20	49
12	18	43
13	16	39
14	15	35
15	14	32
16	13	30
17	13	30
18	12	28
19	11	26
20	11	24
21	10	22
22	10	21
23	9	20
24	9	18
25	9	18
26	8	17
27	8	16
28	8	16

reported in Table IV, can be used together with Table III to define the allowed set of radio configurations enabling the transmission of a data packet of a certain size.

Example: let us consider the transmission of a packet of 1000 bytes. A 20 MHz channel with SCS $\Delta f = 15$ kHz can transport up to 106 PRBs according to Table IV. Then, from Table III it is necessary to use MCS 5 or higher to encode the data packet in a number of PRBs lower than $N^{\text{max}}_{\text{PRB}} = 106$. In particular, the combination of K and N_{sub} must satisfy

$$N^{\star}_{\text{PRB}} \leq K N_{\text{sub}} \leq N^{\text{max}}_{\text{PRB}} \tag{1}$$

for the available channel bandwidth W_{ch} and the selected MCS. Thus, in the example, we could have the couples $\{K = 10, N_{\text{sub}} = 10\}$ or $\{K = 100, N_{\text{sub}} = 1\}$ both leading to $N = 1200$ subcarriers.

C. Resource Allocation

In NR-V2X, two sidelink modes, referred to as Mode 1 and Mode 2, are made available. These modes mirror the controlled and autonomous operation modes, akin to Modes 3 and 4 found in LTE-V2X, respectively. The distinction between these modes lies in the network's involvement in the V2X sidelink communication. In particular, in Mode 1 the presence of the cellular network is mandatory (controlled mode); Mode 2, differently, can operate also in out-of-coverage condition. The two modes can also coexist.

With Mode 1, the NR base station, called *gNodeB*, schedules the resources for V2X sidelink communication, thus network coverage and connection to the base station are required [50].

In Mode 2, the vehicle selects autonomously the sidelink radio resources to use for its transmission, without the support from the network (autonomous mode). The selection is performed among a pre-configured set of resources indicated by the gNodeB [50]. A channel sensing mechanism for selecting resources that are not in use by other vehicles with higher-priority traffic is foreseen. More specifically, the vehicle senses and decodes the sidelink control information (SCI) sent by other vehicles on the sidelink channel (associated to each message), which includes an indication about possible reservation of future resources. The decoded SCIs are stored together with the measurement of the reference signal received power (RSRP) and this information is used to determine which resources must be excluded when a new resource selection is required. After the exclusion process, resources for transmission are selected randomly from the set of the remaining available resources. More details about the overall process can be found in [51].

When operating with the autonomous mode, it is likely that the same pool of resources can be shared (also in part) among different vehicles due to the distributed allocation mechanism. This fact produces interference whose impact must be considered for both communication and sensing.

IV. JCS USING NR-V2X SIDELINK

In this section we first describe the model of the signal that is used for packet transmission in NR-V2X sidelink, and then discuss the use of the same signal for radar sensing, i.e., detection and localization of passive objects in the surroundings. Since also IEEE 802.11p/bd and LTE-V2X signals are based on OFDM, the model described in this section holds for all these technologies. Differences are then relevant when resource allocation and the consequent interference is also considered, which is accounted is Section IV-D. In this regard, we here specifically focus on NR-V2X sidelink, as detailed in Section III.

A. Signal Model

Consider the transmitted OFDM symbol $s_m(t)$, in complex baseband,

$$s_m(t) = \sum_{n=0}^{N-1} \sqrt{P_{n,m}}\, x_{n,m} e^{\text{j}2\pi n \Delta f t}\, \text{rect}\left(\frac{t - mT_{\text{sym}}}{T_{\text{sym}}}\right) \tag{2}$$

where $P_{n,m}$ is the power allocated to the nth subcarrier of the mth symbol and $x_{n,m}$ is the data symbol transmitted in the nth subcarrier of the mth symbol. The symbol time is $T_{\text{sym}} = T + T_{\text{cp}}$ where T_{cp} stands for the cyclic prefix duration and $T = 1/\Delta f$. A total number N of subcarriers and a number M of OFDM symbols are considered for the transmission of a sidelink data packet and, thus, for JCS. We suppose data $x_{n,m}$ arranged in a matrix $\mathbf{X} = \{x_{n,m}\} \in \mathbb{C}^{N \times M}$, where each column represents an OFDM symbol and each row a subcarrier. Assuming $\mathbb{E}\{|x_{n,m}|^2\} = 1$ and equal power allocation, i.e., $P_{n,m} = P_{\text{avg}}$ $\forall n, m$ the average transmitted power is $P_{\text{T}} = N P_{\text{avg}}$.

The vehicle performs sidelink data transmission of the packet to the other vehicles, and the same signal is used for radar sensing. Consider a generic point target in the surroundings

TABLE IV
MAXIMUM NUMBER OF PRBS IN A GIVEN CHANNEL BANDWIDTH W_{CH} FOR DIFFERENT SCS Δf

Δf [kHz]	$N_{\text{PRB}}^{\max}$ per channel BW W_{ch} [MHz]														
	5	10	15	20	25	30	35	40	45	50	60	70	80	90	100
15	25	52	79	106	133	160	188	216	242	270	--	--	--	--	--
30	11	24	38	51	65	78	92	106	119	133	162	189	217	245	273
60	--	11	18	24	31	38	44	51	58	65	79	93	107	121	135

of the transmitting vehicle. The target is assumed located at distance d from the transmitting vehicle, which is concurrently receiving the reflection of its own signal (monostatic radar). The target is also assumed moving with a relative speed v with respect to the transmitting vehicle. The signal received back from the target can be written, in complex baseband, as [52]

$$r(t) = \sum_{m=0}^{M-1} h\, s_m(t-\tau) e^{\mathrm{j}2\pi f_c \nu m T_{\text{sym}}} + n(t) \tag{3}$$

where $\tau = 2\, d/c$ is the delay, $\nu = 2v/c$ is the doppler, with c standing for the speed of light and with f_c indicating the carrier frequency, and $n(t)$ is the additive white Gaussian noise (AWGN) with power spectral density (PSD) $N_0 = k_{\text{B}} T_0 F$, being k_{B} the Boltzmann constant, T_0 the reference temperature, and F the receiver noise figure. The noise power is $P_{\text{n}} = N_0\, W$. Parameters ν and τ are those of interest for the radar processing. The channel coefficient $h = |h| e^{\mathrm{j}\arg h}$ can be written according to the radar equation, resulting in $|h| = \sqrt{P_{\text{R}}/P_{\text{T}}}$ and $\arg h = 2\pi f_c \tau + \phi$, where ϕ accounts for an additional phase shift due to circuits and P_{R} is the received power, given by

$$P_{\text{R}} = P_{\text{T}} \frac{G^2 c^2 \sigma}{(4\pi)^3 f_c^2\, d^4} \tag{4}$$

where G is the antenna gain in the direction of the target. It can be noticed that the path loss is unfavorable with respect to active communication systems due to the two-hop propagation mechanism of radar, presenting a power which scales with the fourth power of the distance. The amount of power backscattered by the target is characterized by its radar cross section (RCS) σ, thus large variations of this parameter are expected depending on the target type.

After standard cyclic prefix removal and FFT processing, we obtain

$$y_{n,m} = \int_{mT_{\text{sym}}+T_{\text{cp}}}^{(m+1)T_{\text{sym}}} r(t)\, e^{-\mathrm{j}2\pi n \Delta f t} \mathrm{d}t \tag{5}$$

which can be written as [52]

$$y_{n,m} = \sqrt{P_{n,m}}\, x_{n,m}\, T\, h e^{-\mathrm{j}2\pi n \Delta f \tau} e^{\mathrm{j}2\pi f_c \nu m T_{\text{sym}}} + z_{n,m} \tag{6}$$

where

$$z_{n,m} = \int_{mT_{\text{sym}}+T_{\text{cp}}}^{(m+1)T_{\text{sym}}} n(t)\, e^{-\mathrm{j}2\pi n \Delta f t} \mathrm{d}t\,. \tag{7}$$

is the noise sample for the mth symbol and nth subcarrier, so that $z_{n,m} \sim \mathcal{CN}(0, \sigma_{\text{n}}^2)$ where $\sigma_{\text{n}}^2 = k_{\text{B}} T_0 F T$.

We define the matrix of received data symbols $\mathbf{Y} = \{y_{n,m}\} \in \mathbb{C}^{N \times M}$. The matrix $\mathbf{Y}$, collected by the radar receiver, is processed to determine the presence of the target and, if present, its distance (range) and speed, through estimation of the parameters τ and ν. Interestingly, according to the signal structure reported in (6), each element $y_{n,m}$ of $\mathbf{Y}$ corresponds to a scaled version of the corresponding TX data symbol multiplied by a couple of phasors. In particular, the target delay produces a linear phase shift among the different subcarriers; differently, the target relative speed produces a linear phase shift among the different OFDM symbols. Hence, radar processing can be realized directly in the *modulated symbols domain*, without the need of operating on the waveform, exploiting efficiently the two-dimensional structure of the OFDM signal [53].

B. Target Detection

The first step accomplished by the radar receiver is the detection of the target. In order to characterize the performance of the target detection step, the classical signal processing scheme usually adopted is here briefly discussed. To detect the target presence, an element-by-element division of the received matrix $\mathbf{Y}$ by the transmitted matrix $\mathbf{X}$ is performed [53], which is known in the monostatic configuration. This way, the dependence of the received matrix from the data is removed. Specifically, we have $\mathbf{R} = \mathbf{Y} \div \mathbf{X}$, with $\mathbf{A} \div \mathbf{B}$ indicating the element-by-element division operation between matrices $\mathbf{A}$ and $\mathbf{B}$ of the same size and where $\mathbf{R} = \{r_{n,m}\} \in \mathbb{C}^{N \times M}$ has entries

$$\begin{aligned} r_{n,m} &= \sqrt{P_{n,m}}\, \alpha\, e^{-\mathrm{j}2\pi n \Delta f \tau} e^{\mathrm{j}2\pi f_c \nu m T_{\text{sym}}} + \widetilde{z}_{n,m} \\ &= u_{n,m} + \widetilde{z}_{n,m} \end{aligned} \tag{8}$$

with $\alpha \triangleq Th$. It is worth noticing that the division for the transmitted data can affect the noise statistic of $\widetilde{z}_{n,m}$ if an alphabet with non-constant envelope is adopted. In order to simplify the analysis, here we assume that $\widetilde{z}_{n,m}$ and $z_{n,m}$ have the same statistic.[3]

The following step for the receiver is to decide, based on the detected energy, about the presence or not of the two complex sinusoids in (8), which lead to the linear phase variations on the received data symbols. Thanks to the decoupling of delay and Doppler, an efficient way for detecting their presence is using a double periodogram, computed along the two directions that correspond to the subcarriers span and the OFDM symbols span [54]. Specifically, the periodogram $\mathbf{E} = \{e_{n,m}\} \in \mathbb{R}^{N \times M}$ is obtained as

$$e_{n,m} = \frac{1}{MN} \left| \sum_{k=0}^{N-1} \left(\sum_{l=0}^{M-1} r_{k,l} e^{-\mathrm{j}2\pi \frac{lm}{M}} \right) e^{\mathrm{j}2\pi \frac{kn}{N}} \right|^2 \tag{9}$$

[3]The reader can refer to [52] for a detailed discussion.

resulting in N fast Fourier transforms (FFTs) and M inverse fast Fourier transforms (IFFTs) operated on the matrix $\mathbf{R}$. Each element of $\mathbf{E}$ is called *bin*; a peak on a specific bin indicates the presence of a target and the corresponding delay and Doppler give indications on the distance and speed. To define if sufficient energy is present in a bin, a comparison with a threshold ξ of the matrix elements of $\mathbf{E}$ can be performed. If at least one periodogram bin is above the threshold ξ, the target is detected; if all the bins are below the threshold, the target is not detected, and the next set of M OFDM symbols and N subcarriers (i.e., the following data packet) is processed. By defining $\mathcal{H}_1$ and $\mathcal{H}_0$ the hypotheses related to the presence and absence of the target, respectively, and the set $\mathcal{D} \triangleq \{(n,m) : e_{n,m} > \xi\}$ with cardinality $|\mathcal{D}|$, the decision rule is given by

$$\text{Decide}: \begin{cases} \widehat{\mathcal{H}}_0; & |\mathcal{D}| = 0 \\ \widehat{\mathcal{H}}_1; & |\mathcal{D}| > 0\,. \end{cases} \tag{10}$$

The threshold value ξ affects the performance of the detection scheme in terms of both probability of detection and probability of false alarm. In fact, a trade-off between the performance in terms of false alarm and detection arises. Low threshold leads to very high probability of detection, but very high probability of false alarm (i.e., decision for the presence of a target, when only noise energy is present); on the contrary, high threshold leads to low probability of false alarm, at the expense of the probability of detection. Thus, the test of interest for target detection is

$$e_{n,m} \underset{\widehat{\mathcal{H}}_0}{\overset{\widehat{\mathcal{H}}_1}{\gtrless}} \xi\,. \tag{11}$$

For further convenience, we distinguish the case whether the target is present or absent, that is

$$e_{n,m} = \begin{cases} \frac{1}{MN}\left|\sum_{k=0}^{N-1}\left(\sum_{l=0}^{M-1}\widetilde{z}_{k,l}\; e^{-\mathrm{j}2\pi\frac{lm}{M}}\right)e^{\mathrm{j}2\pi\frac{kn}{N}}\right|^2; & \mathcal{H}=\mathcal{H}_0 \\ \frac{1}{MN}\left|\sum_{k=0}^{N-1}\left(\sum_{l=0}^{M-1}(u_{k,l}+\widetilde{z}_{k,l})\, e^{-\mathrm{j}2\pi\frac{lm}{M}}\right)e^{\mathrm{j}2\pi\frac{kn}{N}}\right|^2; & \mathcal{H}=\mathcal{H}_1. \end{cases} \tag{12}$$

Considering that a false alarm event occurs when at least one bin is over the threshold in the absence of the target, and thanks to the independence among the energy bins, the probability of false alarm can be written as

$$P_{\text{fa}} = 1 - (1 - p_{\text{fa}})^{NM} \simeq MNp_{\text{fa}} \tag{13}$$

with the single-bin probability of false alarm p_{fa} given by

$$p_{\text{fa}} = \text{Prob}\left\{e_{n,m}^{(\mathcal{H}_0)} > \xi\right\} \tag{14}$$

where $e_{n,m}^{(\mathcal{H}_0)}$ denotes the periodogram bin in the case the target is absent (i.e., only noise is present). Since, in the absence of target, the entries of $\mathbf{E}$ in (12) are obtained as the squared modulus of the sum of MN circularly symmetric Gaussian independent identically distributed (i.i.d.) random variables (R.V.s) with variance σ_{n}^2, their distribution is exponential with parameter $1/\sigma_{\text{n}}^2$; thus, the probability of false alarm per bin p_{fa} is given by the corresponding complementary cumulative distribution function (ccdf) evaluated at ξ, that is

$$p_{\text{fa}} = e^{-\mathsf{TNR}} \tag{15}$$

where we have defined the threshold to noise ratio (TNR) $\mathsf{TNR} = \xi/\sigma_{\text{n}}^2$. In the opposite case, considering that a detection event occurs when at least one bin is over the threshold in the presence of the target, the probability of detection can be written as

$$P_{\text{det}} = \text{Prob}\left\{e_{n,m}^{(\mathcal{H}_1)} > \xi\right\} \tag{16}$$

where $e_{n,m}^{(\mathcal{H}_1)}$ denotes the periodogram bin in the case the target is present. Assuming that the energy of the target is concentrated on a single bin we have $P_{\text{det}} = \text{Prob}\{\tilde{e}_{n,m}^{(\mathcal{H}_1)} > 2\xi/\sigma_{\text{n}}^2\}$ where $\tilde{e}_{n,m}^{(\mathcal{H}_1)} = 2e_{n,m}^{(\mathcal{H}_1)}/\sigma_{\text{n}}^2$. The statistic of the signal-carry bin $\tilde{e}_{n,m}^{(\mathcal{H}_1)}$ is non-central chi-square with two degrees of freedom and non-centrality parameter λ, where

$$\lambda = \frac{2}{MN\sigma_{\text{n}}^2}\left(\sum_{n,m}\sqrt{P_{n,m}}\right)^2 T^2|h|^2 = 2MN\,\mathsf{SNR} \tag{17}$$

and the signal-to-noise ratio (SNR) SNR is defined as the ratio between the received signal power P_{R} and the noise power P_{n}, that is

$$\mathsf{SNR} = \frac{P_{\text{R}}}{P_{\text{n}}} = \frac{P_{\text{R}}}{k_{\text{B}}T_0FW}\,. \tag{18}$$

Therefore, the probability of detection is given by the corresponding ccdf evaluated at ξ, that is

$$P_{\text{det}} = Q_1\left(\sqrt{2MN\,\mathsf{SNR}}, \sqrt{2\,\mathsf{TNR}}\right). \tag{19}$$

with $Q_\xi(\alpha,\beta) = \int_\beta^\infty x\left(\frac{x}{\alpha}\right)^{\xi-1}\exp(-\frac{x^2+\alpha^2}{2})I_{\xi-1}(\alpha x)\,dx$ denoting the generalized Marcum's Q function of order ξ and $I_k(\cdot)$ denoting the kth order modified Bessel function of the first kind [55]. By varying the value of the threshold ξ, different couples $(P_{\text{fa}}, P_{\text{det}})$ can be obtained, depending on the noise and signal intensity, thus drawing the so-called receiver operating characteristic (ROC) curves. As a different approach, the threshold can be also imposed by fixing a specific target probability of false alarm $P_{\text{fa}}^\star$ (constant false alarm rate (CFAR) approach), by inverting the relationships (13) and (15). It is worth noticing that the knowledge (or, for run-time operation, the estimation) of the noise power is required to set the threshold according to the CFAR approach. This strategy is considered in the following.

Interestingly, from (19) it can be noticed that there is an SNR gain equal to MN. In fact, the actual processing gain obtained with the periodogram equals MN since the signal contributions from MN data symbols add coherently, while the noise does not; however, spreading the signal on a larger bandwidth W by increasing the number of subcarriers N increases the noise power accordingly, thus the actual gain is that obtained from the observation of multiple OFDM symbols. Moreover, increasing the number of subcarriers N increases the probability that at least one bin overcomes the threshold: then, in order to keep P_{fa} constant, higher values of the threshold must be considered, thus decreasing the actual probability of detection.

C. Estimation of Target Parameters

We now focus on the estimation quality for range and relative speed between the vehicle and the target.[4] Range estimation $\widehat{d}$ of the distance d between the transmitting vehicle and the target is computed by the estimate $\widehat{\tau}$ of τ as $\widehat{d} = \widehat{\tau}/2c$; similarly, relative speed estimation $\widehat{v}$ of the relative target speed v with respect to that of the transmitting vehicle is computed by the estimate $\widehat{\nu}$ of ν as $\widehat{v} = \widehat{\nu}c/2$. Considering the periodogram $\mathbf{E}$, the coordinates

$$(\widehat{n}, \widehat{m}) = \underset{(n,m)\in\mathcal{D}}{\operatorname{argmax}} \{e_{n,m}\} \tag{20}$$

associated to the maximum bin exceeding the threshold provide coarse estimates $\widehat{\tau}_{\mathrm{c}}$ and $\widehat{\nu}_{\mathrm{c}}$ of the target delay and doppler shift, respectively. The resolution of these coarse estimates is determined by the maximum bandwidth $W = N\Delta f$ and by the overall signal duration MT_{sym}, respectively. Resolution can be improved, for example, via oversampling, by computing FFT/IFFT in (9) with a larger number of points with respect to N and M, thus using zero padding in each row and column of $\mathbf{R}$. Other techniques foresee iterative estimation techniques, starting from a coarse estimate, then refining progressively the search. Regardless of the estimation technique adopted, whose discussion is out of the scope of this paper, the ultimate limit on the radar sensing performance is given by the CRLB on the variance of the range and speed estimation, representing the best performance achievable by any unbiased estimator of these parameters. Considering the signal format (6), the CRLB on the variance of the estimation error for the delay τ, as derived in [52], is given by

$$C_\tau = \frac{3\sigma_{\mathrm{n}}^2}{2P_{\mathrm{avg}}|\alpha|^2\pi^2\Delta f^2 MN(N^2-1)}. \tag{21}$$

Then, substituting $\sigma_{\mathrm{n}}^2 = k_{\mathrm{B}}T_0FT$, $\alpha = Th$, and $P_{\mathrm{avg}} = P_{\mathrm{T}}/N$ and exploiting the definition of SNR in (18), the CRLB on the variance of the estimation error for the range $\widehat{d}$ is

$$\mathsf{CRLB}^{(\widehat{d})} = \frac{3c^2}{8\pi^2\, MN\,\mathsf{SNR}\,(N^2-1)\Delta f^2}. \tag{22}$$

Similarly, according to [52], the CRLB on the variance of the estimation error for the doppler ν is given by

$$C_\nu = \frac{3\sigma_{\mathrm{n}}^2}{2P_{\mathrm{avg}}|\alpha|^2\pi^2 f_{\mathrm{c}}^2\, T_{\mathrm{sym}}^2 MN(M^2-1)}. \tag{23}$$

Then, using the same approach, the CRLB on the variance of the estimation error for the speed $\widehat{v}$ is given by

$$\mathsf{CRLB}^{(\widehat{v})} = \frac{3c^2}{8\pi^2 f_{\mathrm{c}}^2\, MN\,\mathsf{SNR}\,(M^2-1)T_{\mathrm{sym}}^2}. \tag{24}$$

The fundamental factor of merit limiting the range estimation performance in (22) is the squared bandwidth, given approximately by $(N^2-1)\Delta f^2$. Hence, a large SCS Δf and/or a large number of subcarriers N are beneficial for range estimation. Differently, for the relative speed estimation, the fundamental factor of merit limiting the performance in (24) is the squared signal duration given approximately by $(M^2-1)T_{\mathrm{sym}}^2$. As for the target detection case in (19), it can be noticed that the same SNR gain equal to MN is realized in (22) and (24). Again, since spreading the signal on a larger bandwidth W increases the noise power accordingly, the actual gain is that obtained from the observation of multiple OFDM symbols. Differently, increasing N by keeping the bandwidth W fixed (thus decreasing the SCS Δf) is beneficial for both the estimates.

[4] When exploiting JCS in a typical highway scenario, as in the numerical results considered in the following, the detection of the nearby car (e.g., a vehicle ahead of the connected vehicle that performs sensing) and the corresponding ranging estimation is the most important to avoid a collision. Therefore, we consider here the ranging performance only. Target positioning can be realized by estimation of the angle-of-arrival by considering multiple antennas [54], [56].

D. Performance in Multi-User Vehicular Scenarios

We now consider a scenario where a number of vehicles can communicate with each other by relying on NR-V2X sidelink radio technology. The detection probability (19) and the CRLB metrics in (22)–(24) account for the variability in the respective detection/estimation quality due to the randomness of the noise. However, when multiple vehicles are operating in the same environment, thus accessing concurrently to the radio channel for broadcast packet transmission, the sensing performance could be affected by interference. In order to account for this interference effect, we propose here the exploitation of system-level simulations, by accounting for a realistic operating scenario with multiple vehicles and for the resource allocation policies characteristics of NR-V2X sidelink as described in Section III-C. In fact, the distribution of vehicles in the scenario, the resource allocation mechanism, and the packet generation statistic will change the interference level during time, thus affecting consequently the JCS performance.

Let us consider a vehicular scenario, where a number of vehicles are connected through NR-V2X sidelink communications. Let us assume the generic TTI $t \in \mathcal{T}$, where $\mathcal{T}$ is the set of time instants of the simulation, and denote as $\mathcal{I}_t$ the set of vehicles that have a resource allocated in t and a packet to transmit. Each vehicle in $\mathcal{I}_t$ performs its NR-V2X sidelink transmission and radar sensing using the same signal.

To characterize the radar sensing performance in the presence of interference, the signal-to-interference-plus-noise ratio (SINR) related to the signal backscattered by the target of RCS σ at distance d is evaluated as

$$\mathsf{SINR}_{t,i} = \frac{P_{\mathrm{R}}}{P_{\mathrm{n}} + I_{t,i}} \tag{25}$$

where the received power is given by (4). As first approximation, interference from the other vehicles is considered as an additional (Gaussian) noise source, as commonly assumed for communication performance evaluation. In fact, due to the large number of vehicles transmitting at the same time, a possibility is to treat the resulting aggregate interference at the radar receiver as an additional noise [36], [39]. Specifically, the interference at the vehicle i coming from other vehicles transmitting at the same time slot t is accounted by the term $I_{t,i}$, given by

$$I_{t,i} = \sum_{k\in\mathcal{I}_t, k\neq i} \eta_{t,ki}\frac{g_{t,ki}P_{\mathrm{T}}}{L(d_{t,ki})} \tag{26}$$

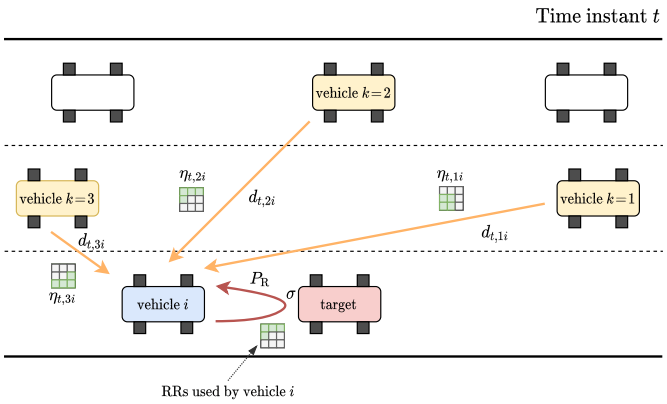

Fig. 2. Pictorial example of the simulation scenario at time instant t. Matrices depict the radio resources used by each vehicle in time (columns) and frequency (rows).

where the term $L(d_{t,ki})$ is the path loss at distance $d_{t,ki}$ between the interfering transmitting vehicle k and the transmitting/sensing vehicle i at slot t, $g_{t,ki}$ is the large-scale fading contribution related to link between the interfering transmitting vehicle k and the transmitting/sensing vehicle i at slot t, $\eta_{t,ki}$ is a coefficient between 0 and 1 accounting for the partial overlap between the resources allocated for the transmission of the vehicle i and that allocated for the transmission of the vehicle k (i.e., interference) also including the in-band emission (IBE) specifications.[5]

Then, radar sensing performance metrics such as CRLBs for range and speed estimation in (22)-(24) can be evaluated for each vehicle in the scenario and for each time slot, considering the SINR (25) instead of the SNR in (18), thus obtaining a set of values $\{\mathsf{CRLB}_{t,i}^{(\widehat{d})}\}$ and $\{\mathsf{CRLB}_{t,i}^{(\widehat{v})}\}$ from which proper statistics can be drawn. For what concerns the detection performance, it is important to underline the fact that the CFAR approach requires the knowledge of the noise power σ_{n}^2; thus, in a variable-noise scenario due to the presence of multiple interferers, achieving the performance resulting from this model will require run-time noise power estimation to properly set the detection threshold η in (11). In particular, by inverting (13) and (15), we have that the TNR is determined directly by the target probability of false alarm $P_{\mathrm{fa}}^{\star}$, according to

$$\mathsf{TNR} \approx -\ln \frac{P_{\mathrm{fa}}^{\star}}{MN} . \tag{27}$$

Thus, fixed the desired false alarm condition, the threshold η is directly proportional to the (variable) noise power and the corresponding probability of detection is expressed by (19) considering the SINR (25).

V. Numerical Results

The performance of NR-V2X radar sensing is characterized by using a system level simulator, realized starting from the open-source simulator WiLabV2Xsim [51]. WiLabV2Xsim is an event driven simulator designed for the investigation of resource allocation techniques for V2X connectivity and implements 5G NR-V2X sidelink. In this work, the simulator was extended for characterizing the radar sensing performance. In particular, per each transmission that is simulated, the procedure performed at the end of the TTI (which is detailed in [51]) allows for the evaluation of the SINR according to (25), which is then exploited to collect the output metrics in terms of probability of detection and CRLBs as detailed in Section IV.

An example of the scenario considered by the simulator is reported in Fig. 2. The ith vehicle is transmitting its packets using sidelink according to a specific set of RRs and jointly performing the sensing of a generic target with RCS σ by listening to the backscattered response. During the same TTI, the set of vehicles $\mathcal{I}_t = \{1, 2, 3\}$ are also transmitting their packets, each using its set of RRs. The set of RRs used by each vehicle is exemplified in the figure using a matrix corresponding to the resources in the time and frequency domains (columns and rows, respectively). The coefficient $\eta_{t,ki}$ indicates the overlap between the resources used by the kth and the ith user in the TTI t; $\eta_{t,ki}$ goes from 0 if they use orthogonal resources (for example vehicles $k = 3$ and i in the figure) to 1 if they completely overlap (for example vehicles $k = 2$ and i in the figure). Depending on $\eta_{t,ki}$ and considering the relative distance between the two nodes $d_{t,ki}$, the path loss $L_{d_{t,ki}}$ is evaluated. Based on these calculations, the interference and the SINR are derived according to (26) and (25), respectively. Finally, the sensing performance is computed, and proper statistics are drawn over the ensemble of vehicles and simulation time instants.

TABLE V
Parameters Adopted for Simulations

Parameter	Symbol	Value
Transmitted power	P_{T}	23 dBm
Antenna gain	G	3 dB
Frequency	f_{c}	5.9 GHz
RX noise figure	F	6 dB
Available channel bandwidth	W_{ch}	40 MHz
SCS	Δf	15, 30, 60 kHz
MCS	--	5, 23
Packet size	--	350, 1000 bytes
Packet generation interval	--	100 ms
# of ODFM symbols	M	14
Average vehicle speed	--	70 km/h
STD of vehicle speed	--	7 km/h
Vehicle density	--	$10 \div 100$ veh./km
Channel model (interference)	--	WINNER+, B1
Shadowing parameter	--	3 dB
Decorrelation distance	--	25 m
Target RCS	σ	$-10, 0, 10$ dBsm
Target probability of false alarm	$P_{\mathrm{fa}}^{\star}$	10^{-4}

A. Simulation Setup

The main settings adopted for the simulations are reported in Table V and discussed hereafter.

We consider a highway scenario with 3 lanes per direction and a variable number of vehicles per kilometer (variable vehicle density). Each vehicle, randomly-deployed at the beginning of the simulation, moves with average speed of 70 km/h and a

[5] In particular, $\eta_{t,ki} = 1$ if exactly the same frequency resources are allocated to both the vehicles i and k at time slot t.

TABLE VI
RESULTING NUMBER OF SUBCARRIERS, TRANSMISSION BANDWIDTH AND TTI FOR THE CONFIGURATIONS CONSIDERED IN SIMULATIONS

Packet	MCS	N_{sub}	N	Δf [kHz]	W [MHz]	TTI [ms]
350	5	4	480	15	7.2	1.0
350	5	4	480	30	14.4	0.5
350	5	4	480	60	28.8	0.25
350	23	1	120	15	1.8	1.0
350	23	1	120	30	3.6	0.5
350	23	1	120	60	7.2	0.25
1000	5	10	1200	15	18	1.0
1000	5	10	1200	30	32	0.5
1000	5	10	1200	60	64	0.25
1000	23	2	240	15	3.6	1.0
1000	23	2	240	30	7.2	0.5
1000	23	2	240	60	14.4	0.25

standard deviation of 7 km/h. Specifically, a straight highway with 3 lanes per direction and a length of 2 km is considered, adopting a wrap-around technique (i.e., a vehicle exiting on one side of the scenario which enters from the other side in the same lane) to support simulations of arbitrary duration [51]. Details on the simulation scenario concerning the traffic pattern used can be found in [57].

Vehicles are supposed equipped with TX/RX antennas with 3 dBi gain and transmitting a fixed power $P_{\text{T}} = 23$ dBm. A receiver with $F = 6$ dB noise figure is considered. The channel between vehicles, for what concerns path loss characterization determining the interference level in (26), is modelled according to the WINNER+, scenario B1, with correlated log-normally distributed shadowing, characterized by a standard deviation of 3 dB and a decorrelation distance of 25 m, as suggested in [58] and commonly adopted. The path loss related to the backscattered channel between the sensing vehicle and the radar target is computed according to (4) since we are considering the detection of the closest target in a line-of-sight (LOS) highway scenario. Ideal full-duplex radios are assumed.

A carrier frequency $f_{\text{c}} = 5.9$ GHz is considered with fixed channel bandwidth W_{ch} to accommodate sidelink signals. W_{ch} is set to 40 MHz to allow considering a large number of configurations in terms of packet size and MCS, as later discussed. All the values of SCS allowed in the sub-6GHz are considered, i.e., 15, 30, and 60 kHz. The subchannel size is set to $K = 10$ PRBs, implying 5 to 22 subchannels in the considered channel bandwidth, depending on the SCS. Regarding the resource allocation, Mode 2 with the same settings as in [51] is adopted. We assume all the users in the scenario adopting the same setup in terms of MCS, SCS, and packet size. Packets are generated every 100 ms; two packet sizes are considered, 350 and 1000 bytes, to simulate typical packets that are used in V2X communication services, e.g. for cooperative awareness message (CAM) and collective perception message (CPM) messages, respectively. MCSs 5 (QPSK) and 23 (64-QAM) are considered. When packets of 350 bytes are transmitted, these are the lowest MCSs to occupy no more than four or one subchannels, respectively. When packets of 1000 bytes are transmitted, two subchannels are occupied with MCS 23; in this case, the MCS 5 does not allow to allocate one packet in one TTI when $\Delta f = 60$ kHz, since this would not fit the available channel bandwidth W_{ch}. The resulting number of subcarriers, the transmission bandwidths, and the TTIs related to the different configurations, are reported in Table VI . Of course, the small bandwidth will result in a quite poor resolution; however, the short vehicle-target distance, thanks to the radar performed at the vehicle side, will lead typically to high SNR conditions, thus low values of the bound, as shown in the following results. It is worth noticing that the small bandwidth could determine a performance degradation in the case of strong multipath, as also highlighted for V2X sidelink active localization [59].

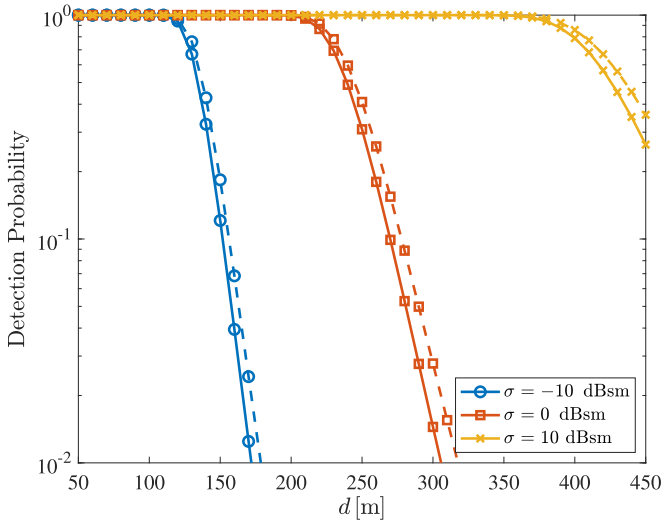

Fig. 3. Probability of detection as a function of the distance d from the target varying the RCS. Continuous lines (–) are for MCS 5; dashed lines (- -) are for MCS 23.

B. Sensing Performance in Interference-Free Condition

In this section, we present numerical results in the absence of interference to be used as benchmark.

Fig. 3 shows the probability of detection as a function of the distance d from the target varying the RCS as $\sigma = \{-10, 0, 10\}$ dBsm, which are example of values for pedestrians, motorcycles, and car, respectively [60]. A packet of 1000 bytes is assumed. MCSs 5 and 23 are considered, with SCS $\Delta f = 15$ kHz. According to Table III, MCS 5 leads to $K = 10$ and $N_{\text{sub}} = 10$ (i.e., $N = 1200$ subcarriers and a bandwidth of $W = 18$ MHz). Differently, MCS 23 leads to $K = 10$ and $N_{\text{sub}} = 2$ (i.e., $N = 240$ subcarriers and a bandwidth of $W = 3.6$ MHz), resulting in a lower spectrum occupation. Results are obtained by selecting a threshold η guaranteeing a probability of false alarm $P_{\text{fa}} = 10^{-4}$. As it is possible to see from Fig. 3, decreasing N is slightly beneficial for the detection quality. In fact, lower N allows the use of a lower threshold η (i.e., lower TNR), thus augmenting the probability of detection. In general, it is possible to see that even the targets with small RCS can be detected at quite a large distance from the vehicle; this is due to the coherent accumulation of the MN contributions, producing a significant processing gain in the SNR (in the examples, 35 dB for $N = 240$ and 42 dB for $N = 1200$, respectively). In Fig. 4, the CRLB for distance estimation is reported, in the same setup of the figure above. In this case it can be seen how the performance is impacted by the MCS, i.e. by the number of subcarriers. Here increasing the MCS has a negative effect

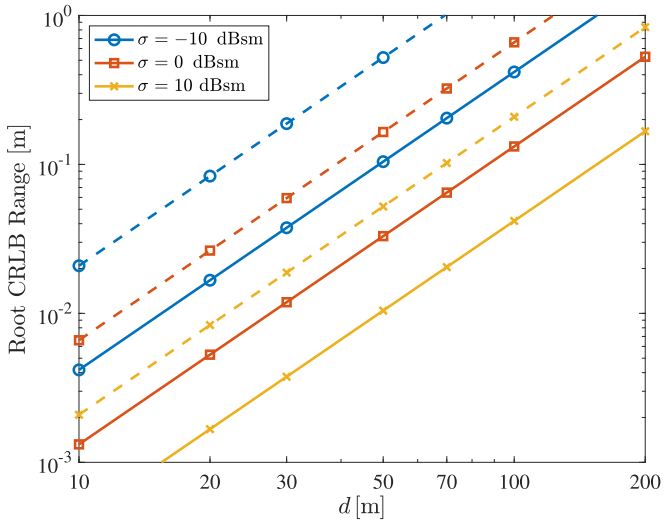

Fig. 4. CRLB for distance estimation as a function of the distance d from the target varying the RCS. Continuous lines (–) are for MCS 5; dashed lines (- -) are for MCS 23.

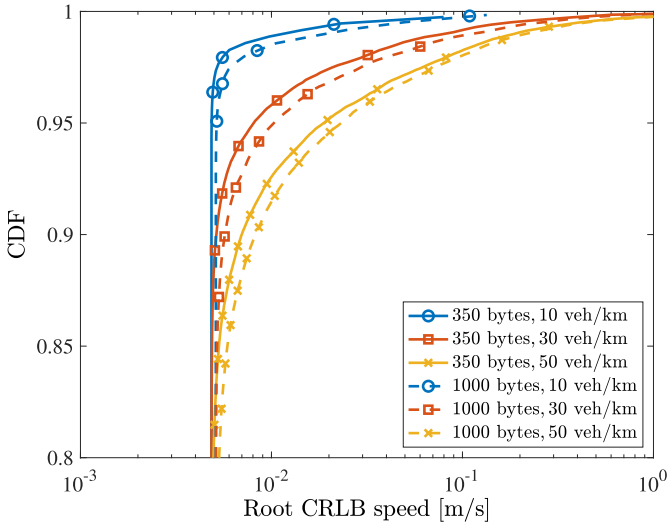

Fig. 6. Empirical CDF of the root CRLB for speed estimation, varying the packet size and the vehicle density, with MCS 23, $\Delta f = 15$ kHz.

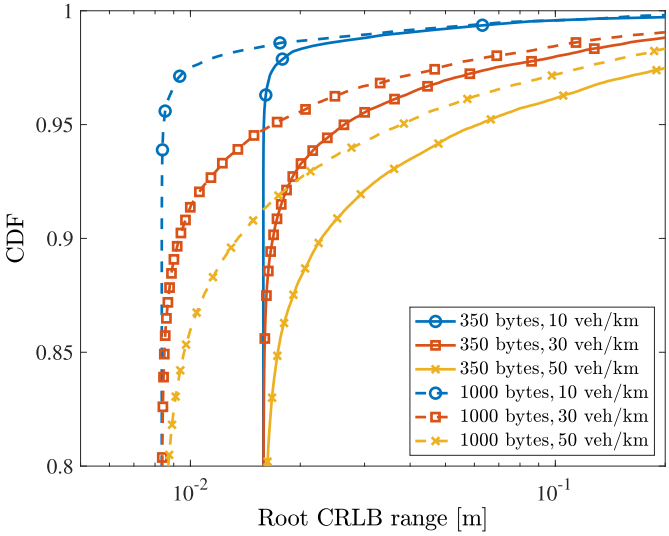

Fig. 5. Empirical CDF of the root CRLB for range estimation, varying the packet size and the vehicle density, with MCS 23, $\Delta f = 15$ kHz.

on the performance, since the bandwidth W decreases accordingly. In general, distance estimation performance is quite poor for distances larger than 100 m, due to the limited bandwidth considered. It is fundamental to observe the fact that these results are obtained in a single-vehicle scenario. When multiple vehicles share the same wireless medium, performance could be severely limited by reciprocal interference, as characterized in the following section.

C. Impact of Interference

In this section, we consider the effect of interference on the sensing performance by accounting for multiple vehicles in the scenario and resource allocation policies of 5G NR-V2X sidelink. A RCS $\sigma = 10$ dBsm is assumed.

Fig. 5 shows the empirical CDF of the root CRLB for the range estimation varying the packet size and the vehicle density. Results are obtained at a distance $d = 20$ m from the target, with MCS 23 and SCS $\Delta f = 15$ kHz. Results confirm how the transmission of a larger packet improves the estimation performance, thanks to the larger bandwidth. Moreover, it can be noticed how the increase of the vehicle density reduces the accuracy due to the increased interference level. It can be noticed that for 1000 bytes (- -), the vertical asymptote at about 0.85 cm accuracy corresponds to the interference-free case which can be obtained by Fig. 4 in the same setting (yellow dashed at $d = 20$ m).

Fig. 6 shows the empirical CDF of the root CRLB for the speed estimation varying the packet size and the vehicle density. In this case, the squared signal duration $(M^2 - 1)T_{\text{sym}}^2$ is the same for all configurations (i.e., constant TTI), so that no impact from this factor is expected according to (24). In the absence of interference, as discussed in Section IV, no benefits are experienced by increasing the number of subcarriers thus considering larger packets (with fixed SCS). Here it can be observed that, differently from the interference-free condition, the transmission of a larger packet is not beneficial for the speed estimation and degrades the performance. Indeed, the transmission of a smaller packet is more robust to an increase of the vehicle density (thus, interference) as it occupies less frequency resources, leading to a higher SINR. In any condition, an increase of the vehicle density decreases the accuracy.

Starting from the CDFs behaviour in Fig. 5, we now focus on the 95-percentile of the root CRLB as performance metric. In Fig. 7 the impact of the MCS and the SCS is investigated, reporting the root-CRLB as a function of the distance d from the target, for packets of 350 bytes. A density of 30 vehicles per km is assumed. Analogously to the interference-free case, increasing the bandwidth through an increase of the SCS and/or a lower MCS is beneficial for the estimation quality. The larger improvement is obtained for SCS $\Delta f = 60$ kHz, thanks to the inverse proportionality of the CRLB with the square of the bandwidth. Interestingly, the same performance is obtained for MCS 5 with SCS 15 kHz ($W = 7.2$ MHz) and for MCS 23 with

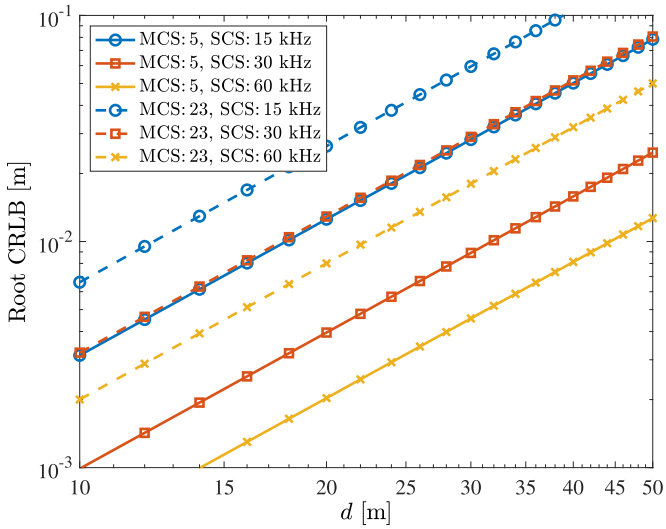

Fig. 7. 95-percentile of the root-CRLB for range estimation as a function of the distance d from the target, varying MCS and SCS; the packet size is 350 bytes. The vehicular density is 30 veh/km.

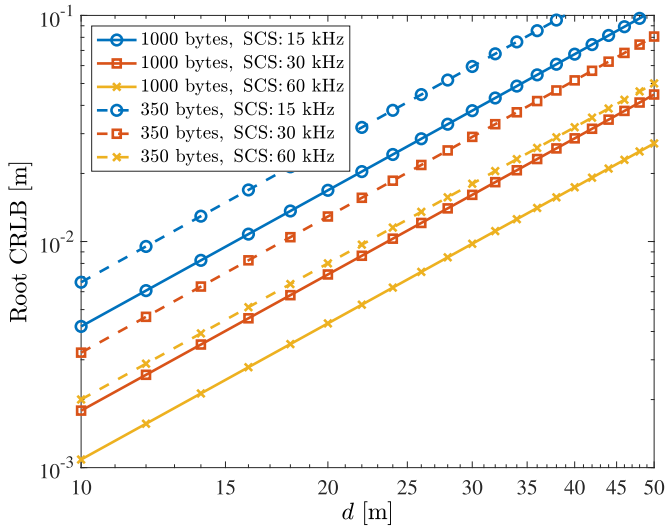

Fig. 8. 95-percentile of the root-CRLB for range estimation as a function of the distance d from the target varying the packet size and the SCS, with MCS 23. The vehicular density is 30 veh/km.

SCS 30 kHz ($W = 3.6$ MHz). In this case, larger bandwidth does not translate in improved performance, due to the effect of interference. In fact, the channel occupation of the first configuration is higher, as it will be evident with the following up analysis, leading to higher probability of collision and then poorer SINR.

Fig. 8 shows the root-CRLB for range estimation as a function of the distance d from the target, considering a density of 30 vehicles per km, MCS 23, and varying the packet size and the SCS. Under the same packet size, the widening of the SCS leads to a larger transmission bandwidth, therefore the CRLB is lower for increasing values of SCS, both for the 1000 and 350 bytes, as highlighted also in Fig. 7. Similarly, moving from 350 to 1000 bytes packets improves the performance. Notice that a packet size of 1000 bytes with SCS 15 kHz has a worse performance than a packet size of 350 bytes with SCS 30 kHz, despite the two configurations occupying the same bandwidth $W = 3.6$ MHz. The latter, in fact, corresponds to larger TTI, thus it suffers more from interference.

The following results, shown in Fig. 9, consider at the same time the sensing and the communication performance, with the joint use of the same waveform. Moreover, the impact of the vehicle density (i.e., of the interference level) is characterized. Specifically, Fig. 9 shows, assuming 350 bytes packets and varying the SCS and the MCS, *(i)* the 95-percentile root-CRLB at $d = 20$ m, *(ii)* the packet error rate calculated as the average at all the receivers within 300 m from the transmitters, and *(iii)* the channel busy ratio averaged in time and among the vehicles. The channel busy ratio is defined as the ratio of sub-channels that experience a power level higher than a certain threshold to the total number of sub-channels in the previous 100 subframes [25], thus indicating the level of congestion of the radio resources. More details on the calculation of this metric and the packet error rate in the simulator can be found in [51]. Fixing the MCS (i.e., considering either continuous or dashed lines), the use of a larger SCS is always beneficial for range estimation (lower CRLB), thanks to the larger bandwidth. Differently, this is not always true when fixing the SCS (i.e., the color of the curves). In this case, with $\Delta f = 30$ kHz and $\Delta f = 60$ kHz, when the vehicle density is low it is preferable to use the lower MCS (i.e., larger bandwidth). Contrarily, when the vehicle density is large, the higher MCS becomes preferable. In fact, as it can be inferred by looking at the channel busy ratio, the channel is much more occupied when packets with low MCS are considered (e.g., assuming SCS $\Delta f = 60$ kHz, the channel busy ratio goes from 0.1 to 0.2 when the MCS moves from 23 to 5); this implies that the interference increases relevantly, and this counteracts the benefit of the larger bandwidth. To remark the impact of interference, let us focus, as an example, to the curves for $\Delta f = 60$ kHz / MCS 23 (yellow dashed) and $\Delta f = 30$ kHz / MCS 5 (red continuous). With these configurations we have, from Table VI, that the bandwidth is $W = 7.2$ MHz ($N = 120$) and $W = 14.4$ MHz ($N = 480$), respectively. It follows, as discussed with the analysis of the CRLB in Section IV-C, that the second configuration (red continuous) should be beneficial for range estimation. From Fig. 9 it can be noticed that, in fact, this is the case, but only at low vehicle density. When the density increases, the higher channel occupation, which is visible in terms of channel busy ratio, implies a higher interference and consequently a lower performance of the sensing. Finally, the average error rate shown in Fig. 9 allows to investigate how the communication performance is impacted by the same parameters considered for sensing performance evaluation. In particular, the large MCS (dashed curves) is less favorable since it requires larger SINR to correctly decode the packets (i.e., smaller transmission range), despite in general it suffers less the interference (lower channel busy ratio than the corresponding curves for low MCS). When low MCS is considered (continuous curves) the benefit of using low or high SCS depends on the interference level. In general, the interplay between packet size, bandwidth, number of subcarriers, MCS, SCS must be carefully considered in relationship with the actual

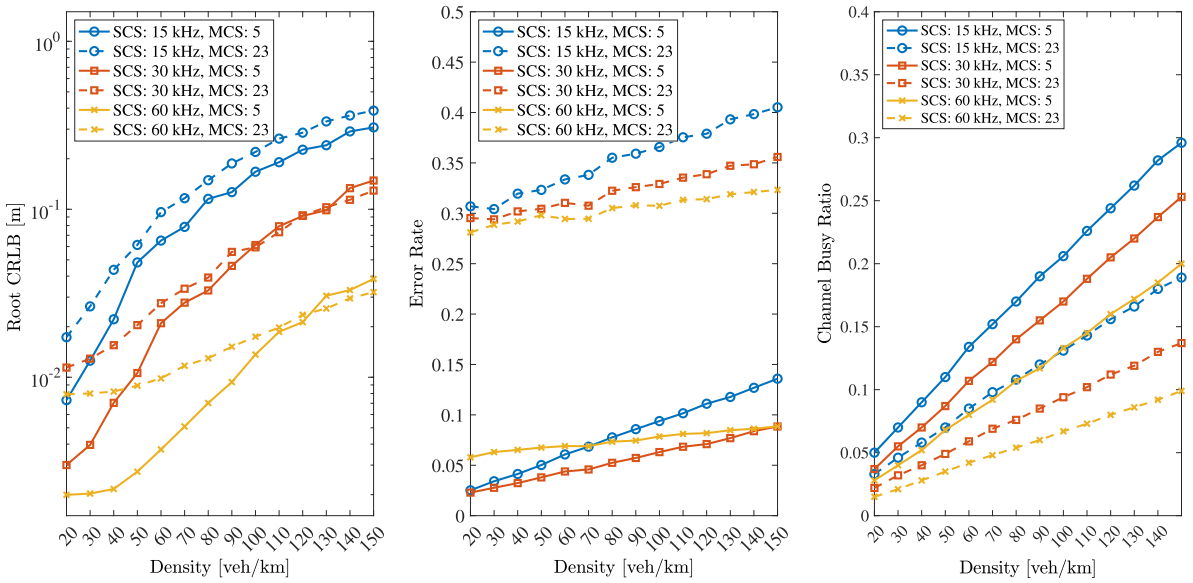

Fig. 9. 95-percentile of the root-CRLB, packet error rate, and channel busy ratio, as a function of the vehicle density, with packet size 350 bytes.

vehicle density, to obtain reliable performance for both communication and sensing.

VI. Conclusion

We investigated the use of 5G NR-V2X sidelink signals for joint communication and sensing, by presenting a method for the evaluation of the performance in realistic conditions with multiple connected vehicles. Specifically, we focused on the impact of interference and resource allocation policies on the radar sensing performance in terms of estimation accuracy for the target parameters (i.e., range and relative speed). We also correlated the communication performance, in terms of average packet error rate and channel busy ratio, to the radar sensing performance, showing the impact of MCS, SCS, packet size, and vehicle density. The work highlighted the notable effects of interference, affecting the behavior of parameters' estimation quality differently with respect to interference-free conditions (e.g., impact of the bandwidth on range estimation) thus showing that the operating context (number of vehicles, resource allocation policies, etc.) has to be carefully accounted for both communication and sensing performance evaluation.

Acknowledgment

Authors would link to thank Vittorio Todisco and Caterina Giovannetti for the support with the simulations.

References

[1] "Cisco annual internet report 2018–2023," Mar. 2020. [Online]. Available: https://www.cisco.com/c/en/us/solutions/collateral/executive-perspectives/annual-internet-report/white-paper-c11-741490.html

[2] A. Bazzi, A. O. Berthet, C. Campolo, B. M. Masini, A. Molinaro, and A. Zanella, "On the design of sidelink for cellular V2X: A literature review and outlook for future," *IEEE Access*, vol. 9, pp. 97953–97980, 2021.

[3] L. Montero, C. Ballesteros, C. De Marco, and L. Jofre, "Beam management for vehicle-to-vehicle (V2V) communications in millimeter wave 5G," *Veh. Commun.*, vol. 34, 2022, Art. no. 100424. [Online]. Available: https://www.sciencedirect.com/science/article/pii/S2214209621000930

[4] W. Yuan, Z. Wei, S. Li, J. Yuan, and D. W. K. Ng, "Integrated sensing and communication-assisted orthogonal time frequency space transmission for vehicular networks," *IEEE J. Sel. Topics Signal Process.*, vol. 15, no. 6, pp. 1515–1528, Nov. 2021.

[5] H. Wymeersch et al., "Integration of communication and sensing in 6G: A joint industrial and academic perspective," in *Proc. IEEE Int. Symp. Pers., Indoor, Mobile Radio Commun.*, 2021, pp. 1–7.

[6] Q. Wang, A. Kakkavas, X. Gong, and R. A. Stirling-Gallacher, "Towards integrated sensing and communications for 6G," in *Proc. IEEE Int. Symp. Joint Commun. Sens.*, 2022, pp. 1–6.

[7] D. Tagliaferri et al., "Integrated sensing and communication system via dual-domain waveform superposition," *IEEE Trans. Wireless Commun.*, early access, Sep. 26, 2023, doi: 10.1109/TWC.2023.3316888.

[8] C. B. Barneto, S. D. Liyanaarachchi, M. Heino, T. Riihonen, and M. Valkama, "Full duplex radio/radar technology: The enabler for advanced joint communication and sensing," *IEEE Wireless Commun.*, vol. 28, no. 1, pp. 82–88, Feb. 2021.

[9] L. Pucci, E. Matricardi, E. Paolini, W. Xu, and A. Giorgetti, "Performance analysis of a bistatic joint sensing and communication system," in *Proc. IEEE Int. Conf. Commun. Workshops*, 2022, pp. 73–78.

[10] S. Roudiere, V. Martinez, and D. Delahaye, "Orientation based band sharing for radar interference mitigation," in *Proc. IEEE Veh. Technol. Conf.*, 2023, pp. 1–6.

[11] C. Aydogdu et al., "Radar interference mitigation for automated driving: Exploring proactive strategies," *IEEE Signal Process. Mag.*, vol. 37, no. 4, pp. 72–84, Jul. 2020.

[12] T. Wild, V. Braun, and H. Viswanathan, "Joint design of communication and sensing for beyond 5G and 6G systems," *IEEE Access*, vol. 9, pp. 30845–30857, 2021.

[13] S. D. Liyanaarachchi, C. B. Barneto, T. Riihonen, and M. Valkama, "Experimenting joint vehicular communications and sensing with optimized 5G NR waveform," in *Proc. IEEE Veh. Technol. Conf.*, 2021, pp. 1–5.

[14] T. Shimizu, V. Va, G. Bansal, and R. W. Heath, "Millimeter wave V2X communications: Use cases and design considerations of beam management," in *Proc. Asia-Pacific Microw. Conf.*, 2018, pp. 183–185.

[15] J. Shen et al., "mmV2V: Combating one-hop multicasting in millimeter-wave vehicular networks," in *Proc. IEEE 42nd Int. Conf. Distrib. Comput. Syst.*, 2022, pp. 735–742.

[16] D. Tagliaferri, M. Mizmizi, D. Badini, C. Mazzucco, and U. Spagnolini, "Multi-vehicular beam space learning for channel estimation in 6G V2X systems," in *Proc. IEEE Int. Workshop Signal Process. Adv. Wireless Commun.*, 2021, pp. 46–50.

[17] W. U. Khan, F. Jameel, N. Kumar, R. Jäntti, and M. Guizani, "Backscatter-enabled efficient V2X communication with non-orthogonal multiple access," *IEEE Trans. Veh. Technol.*, vol. 70, no. 2, pp. 1724–1735, Feb. 2021.

[18] R. Chattopadhyay and C.-K. Tham, "Joint sensing and processing resource allocation in vehicular ad-hoc networks," *IEEE Trans. Intell. Veh.*, vol. 8, no. 1, pp. 616–627, Jan. 2023.

[19] L. Reichardt, C. Sturm, F. Grünhaupt, and T. Zwick, "Demonstrating the use of the IEEE 802.11p car-to-car communication standard for automotive radar," in *Proc. Eur. Conf. Antennas Propag.*, 2012, pp. 1576–1580.

[20] B. Kihei, J. A. Copeland, and Y. Chang, "Design considerations for vehicle-to-vehicle IEEE 802.11p radar in collision avoidance," in *Proc. IEEE Glob. Commun. Conf.*, 2015, pp. 1–7.

[21] K. U. Mazher, T. Shimizu, R. W. Heath, and G. Bansal, "Automotive radar using IEEE 802.11p signals," in *Proc. IEEE Wireless Commun. Netw. Conf.*, 2018, pp. 1–6.

[22] K. Ganesan, J. Lohr, P. B. Mallick, A. Kunz, and R. Kuchibhotla, "NR sidelink design overview for advanced V2X service," *IEEE Internet Things Mag.*, vol. 3, no. 1, pp. 26–30, Mar. 2020.

[23] G. Naik, B. Choudhury, and J. Park, "IEEE 802.11bd and 5G NR V2X: Evolution of radio access technologies for V2X communications," *IEEE Access*, vol. 7, pp. 70169–70184, 2019.

[24] S. Gyawali, S. Xu, Y. Qian, and R. Q. Hu, "Challenges and solutions for cellular based V2X communications," *IEEE Commun. Surv. Tuts.*, vol. 23, no. 1, pp. 222–255, Firstquarter 2021.

[25] M. H. C. Garcia et al., "A tutorial on 5G NR V2X communications," *IEEE Commun. Surv. Tuts.*, vol. 23, no. 3, pp. 1972–2026, Thirdquarter 2021.

[26] P. Kumari, J. Choi, N. González-Prelcic, and R. W. Heath, "IEEE 802.11ad-based radar: An approach to joint vehicular communication-radar system," *IEEE Trans. Veh. Technol.*, vol. 67, no. 4, pp. 3012–3027, Apr. 2018.

[27] P. Kumari, N. J. Myers, and R. W. Heath, "Adaptive and fast combined waveform-beamforming design for mmwave automotive joint communication-radar," *IEEE J. Sel. Topics Signal Process.*, vol. 15, no. 4, pp. 996–1012, Jun. 2021.

[28] C. D. Ozkaptan, E. Ekici, O. Altintas, and C.-H. Wang, "OFDM pilot-based radar for joint vehicular communication and radar systems," in *Proc. IEEE Veh. Netw. Conf.*, 2018, pp. 1–8.

[29] C. D. Ozkaptan, E. Ekici, and O. Altintas, "DEMO: A software-defined OFDM radar for joint automotive radar and communication systems," in *Proc. IEEE Veh. Netw. Conf.*, 2019, pp. 1–2.

[30] C.-H. Wang, O. Altintas, C. D. Ozkaptan, and E. Ekici, "Multi-range joint automotive radar and communication using pilot-based OFDM radar," in *Proc. IEEE Veh. Netw. Conf.*, 2020, pp. 1–4.

[31] M. Lübke, J. Fuchs, V. Shatov, A. Dubey, R. Weigel, and F. Lurz, "Combining radar and communication at 77 GHz using a CDMA technique," in *Proc. IEEE MTT-S Int. Conf. Microw. Intell. Mobility*, 2020, pp. 1–4.

[32] V. Petrov, G. Fodor, S. Andreev, H. Do, and H. Sahlin, "V2X connectivity: From LTE to joint millimeter wave vehicular communications and radar sensing," in *Proc. 53rd Asilomar Conf. Signals, Syst., Comput.*, 2019, pp. 1120–1124.

[33] F. Liu, W. Yuan, C. Masouros, and J. Yuan, "Radar-assisted predictive beamforming for vehicular links: Communication served by sensing," *IEEE Trans. Wireless Commun.*, vol. 19, no. 11, pp. 7704–7719, Nov. 2020.

[34] Y. Liu, G. Liao, Y. Chen, J. Xu, and Y. Yin, "Super-resolution range and velocity estimations with OFDM integrated radar and communications waveform," *IEEE Trans. Veh. Technol.*, vol. 69, no. 10, pp. 11659–11672, Oct. 2020.

[35] X. Cheng, D. Duan, S. Gao, and L. Yang, "Integrated sensing and communications (ISAC) for vehicular communication networks (VCN)," *IEEE Internet Things J.*, vol. 9, no. 23, pp. 23441–23451, Dec. 2022.

[36] C. D. Ozkaptan, E. Ekici, C.-H. Wang, and O. Altintas, "Optimal precoder design for MIMO-OFDM-based joint automotive radar-communication networks," in *Proc. Int. Symp. Model. Optim. Mobile, Ad Hoc, Wireless Netw.*, 2021, pp. 1–8.

[37] Z. Ni, J. A. Zhang, K. Yang, and R. Liu, "Frequency-hopping based joint automotive radar-communication systems using a single device," in *Proc. IEEE Int. Conf. Commun. Workshops*, 2022, pp. 480–485.

[38] S. Wang, R. Chen, L. Zhao, and C. Liu, "Millimeter wave integrated sensing and communication with hybrid architecture in vehicle to vehicle network," in *Proc. IEEE 94th Veh. Technol. Conf.*, 2021, pp. 01–06.

[39] Q. Zhang, X. Wang, Z. Li, and Z. Wei, "Design and performance evaluation of joint sensing and communication integrated system for 5G mmWave enabled CAVs," *IEEE J. Sel. Topics Signal Process.*, vol. 15, no. 6, pp. 1500–1514, Nov. 2021.

[40] C. B. Barneto et al., "Beamforming and waveform optimization for OFDM-based joint communications and sensing at mmWaves," in *Proc. Asilomar Conf. Signals, Syst., Comput.*, 2020, pp. 895–899.

[41] S. Bartoletti, N. Decarli, and B. M. Masini, "Sidelink 5G-V2X for integrated sensing and communication: The impact of resource allocation," in *Proc. IEEE Int. Conf. Commun. Workshops*, 2022, pp. 79–84.

[42] N. Decarli, S. Bartoletti, and B. M. Masini, "Joint communication and sensing in 5G-V2X vehicular networks," in *Proc. IEEE Mediterranean Electrotech. Conf.*, 2022, pp. 295–300.

[43] R. Molina-Masegosa, J. Gozalvez, and M. Sepulcre, "Comparison of IEEE 802.11p and LTE-V2X: An evaluation with periodic and aperiodic messages of constant and variable size," *IEEE Access*, vol. 8, pp. 121526–121548, 2020.

[44] G. Naik, B. Choudhury, and J.-M. Park, "IEEE 802.11bd & 5G NR V2X: Evolution of radio access technologies for V2X communications," *IEEE Access*, vol. 7, pp. 70169–70184, 2019.

[45] Z. Wu, S. Bartoletti, V. Martinez, V. Todisco, and A. Bazzi, "Analysis of co-channel coexistence mitigation methods applied to IEEE 802.11p and 5G NR-V2X sidelink," *Sensors*, vol. 23, no. 9, 2023, Art. no. 4337. [Online]. Available: https://www.mdpi.com/1424-8220/23/9/4337

[46] "Study on enhancement of 3GPP support for 5G V2X services; Release 16," 3GPP, Sophia Antipolis, France, Tech. Rep. 22.886, Dec. 2018.

[47] "Technical specification group services and system aspects. enhancement of 3GPP support for V2X scenarios Release 15," 3GPP, Sophia Antipolis, France, Tech. Rep. 22.186, Jun. 2019.

[48] C. Campolo, A. Molinaro, F. Romeo, A. Bazzi, and A. O. Berthet, "5G NR V2X: On the impact of a flexible numerology on the autonomous sidelink mode," in *Proc. IEEE 5G World Forum*, 2019, pp. 102–107.

[49] T. Das et al., "CoReCast: Collision resilient broadcasting in vehicular networks," in *Proc. 16th Annu. Int. Conf. Mobile Syst., Appl., Serv.*, 2018, pp. 217–229.

[50] "Overall description of radio access network (RAN) aspects for vehicle-to-everything (V2X) based on LTE and NR; Release 16," 3GPP, Sophia Antipolis, France, Tech. Rep. 37.895, Jul. 2020.

[51] V. Todisco, S. Bartoletti, C. Campolo, A. Molinaro, A. O. Berthet, and A. Bazzi, "Performance analysis of sidelink 5G-V2X mode 2 through an open-source simulator," *IEEE Access*, vol. 9, pp. 145648–145661, 2021.

[52] M. F. Keskin, V. Koivunen, and H. Wymeersch, "Limited feedforward waveform design for OFDM dual-functional radar-communications," *IEEE Trans. Signal Process.*, vol. 69, pp. 2955–2970, 2021.

[53] C. Sturm and W. Wiesbeck, "Waveform design and signal processing aspects for fusion of wireless communications and radar sensing," *Proc. IEEE*, vol. 99, no. 7, pp. 1236–1259, Jul. 2011.

[54] L. Pucci, E. Paolini, and A. Giorgetti, "System-level analysis of joint sensing and communication based on 5G new radio," *IEEE J. Sel. Areas Commun.*, vol. 40, no. 7, pp. 2043–2055, Jul. 2022.

[55] M. Abramowitz and I. A. Stegun, *Handbook of Mathematical Functions Wih Formulas, Graphs, and Mathematical Tables*. Washington, DC, USA: United States Dept. Commerce, 1970.

[56] C. Giovannetti, N. Decarli, S. Bartoletti, R. A. Stirling-Gallacher, and B. M. Masini, "Target positioning accuracy of V2X sidelink joint communication and sensing," *IEEE Wireless Commun. Lett.*, early access, Dec. 25, 2023, doi: 10.1109/LWC.2023.3346937.

[57] "Study on evaluation methodology of new vehicle-to-everything (V2X) use cases for LTE and NR," 3GPP, Sophia Antipolis, France, Tech. Rep. 37.885, Jun. 2019.

[58] "Technical specification group radio access network; study on LTE-based V2X services; Release 14," 3GPP, Sophia Antipolis, France, Tech. Rep. 36.885, Jul. 2016.

[59] Y. Ge et al., "Analysis of V2X sidelink positioning in sub-6 GHz," in *Proc. Int. Symp. Joint Commun. Sens.*, 2023, pp. 1–6.

[60] "System reference document (SRdoc); Transmission characteristics; Technical characteristics for radiodetermination equipment for ground based vehicular applications within the frequency range 77 GHz to 81 GHz," ETSI, Sophia Antipolis, France, Tech. Rep. 103 593, 2020.

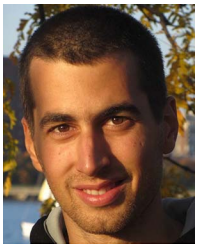

Nicolò Decarli (Member, IEEE) received the Ph.D. degree in electronics, telecommunications, and information technologies from the University of Bologna, Bologna, Italy, in 2013. In 2012, he was a Visiting Student with the Wireless Communication and Network Sciences Laboratory, Massachusetts Institute of Technology, Cambridge, MA, USA. He is currently a Researcher with the Institute of Electronics, Computer, and Telecommunication Engineering, National Research Council of Italy. His research interests include wireless communication theory, radio localization, ultra-wide bandwidth systems, and radio frequency identification. In 2011, he served on the Local Organization Committee of the IEEE International Conference on Ultra-Wideband. He was the TPC Co-Chair of the 2018 IEEE ICC Workshop on Advances in Network Localization and Navigation and the Track-Chair of the 2018 IEEE International Symposium on Personal, Indoor, and Mobile Radio Communications.

Stefania Bartoletti (Member, IEEE) received the Laurea degree (*summa cum laude*) in electronics and telecommunications engineering and the Ph.D. degree in information engineering from the University of Ferrara, Ferrara, Italy, in 2011 and 2015, respectively. She is currently an Associate Professor with the University of Rome, Tor Vergata, Italy. Dr. Bartoletti was awarded a Starting Grant in 2023 from the European Research Council. From 2019 to 2022, she was a Researcher with the Institute of Electronics, Computer and Telecommunication Engineering of the National Research Council of Italy. From 2016 to 2019, she was a Marie Skłodowska-Curie Global Fellow within the Horizon 2020 European Framework with the Massachusetts Institute of Technology, Cambridge, MA, USA, and the University of Ferrara. Her research interests include theory and experimentation of wireless networks for sensing and localization. She was the recipient of the 2016 Paul Baran Young Scholar Award of the Marconi Society. She was the Chair of the Technical Program Committee (TPC) for several IEEE ICC and Globecom Workshops, track Chair at IEEE VTC 2024, and a reviewer for numerous IEEE journals and international conferences. She is an Editor of IEEE COMMUNICATIONS LETTERS.

Alessandro Bazzi (Senior Member, IEEE) is currently an Associate Professor with the University of Bologna, Bologna, Italy, and co-founder of CNIT/WiLab. From 2002 to 2019, he was a Researcher of the National Research Council of Italy (CNR). His research interests include medium access control and radio resource management of wireless networks, with particular focus on connected and autonomous vehicles (CAVs). During 2020–2022, he had been part of the ETSI Specialist Task Force developing the set of standards related to multichannel operations in the ITS band. He participated to several conferences as tutorial instructor or panelist (including IEEE ICC 2021 and Globecom 2021), as kenoyte speaker at ICUMT 2020, and he organized Special Sessions or Workshops at IEEE PIMRC 2018 and 2019. He is currently Chief Editor of Hindawi Mobile Information Systems.

Richard A. Stirling-Gallacher (Member, IEEE) received the M.Eng. degree in electronic engineering from the University of Southampton, Southampton, U.K., in 1990, and the Ph.D. degree from The University of Edinburgh, Edinburgh, U.K., in 1997. From 1997 to 2012, he was a Principal Researcher with Sony Deutschland GmbH, Stuttgart, Germany, where he led wireless system and algorithmic research for 3G, 4G, and millimeter-wave (mm-wave)-based communication systems. From 2012 to 2014, he was with Samsung Research America, Dallas, TX, USA, where he led research and pre-standardization for mm-wave and massive multi in multi out (MIMO) for 5G NR. He joined Huawei Technologies Inc., San Diego, CA, USA, in 2014, and subsequently in 2017, transferred to Munich Research Center, Huawei Technologies Duesseldorf GmbH, Munich, Germany, as a Research Expert/Team Leader. He holds more than 125 granted U.S. patents and is the Vice Chair for the ETSI ISG on ISAC. His interests include ISAC, positioning, massive MIMO, and V2X for 6G communication systems.

Barbara M. Masini (Senior Member, IEEE) received the Laurea degree (*summa cum laude*) and the Ph.D. degree in telecommunications engineering from the University of Bologna, Bologna, Italy, in 2001 and 2005, respectively. She is currently a Senior Researcher with the Institute for Electronics and for Information and Telecommunications Engineering of the National Research Council of Italy. She is also an Adjunct Professor with the University of Bologna and an Associate Member of CNIT/Wilab, Italy. She works in the area of wireless communication systems. Her research interests include connected vehicles, from physical and MAC levels aspects up to applications and field trial implementations, relay assisted communications, energy harvesting, and visible light communication. She is the Editor of IEEE ACCESSand *Computer Communication* (Elsevier). She is responsible for a number of National and International Projects on Vehicular Communications and Urban Intelligence and responsible of the design and test of field trials on cooperative connected vehicles.

Open Access provided by 'Consiglio Nazionale delle Ricerche-CARI-CARE-ITALY' within the CRUI CARE Agreement